Divergent El Niño responses to volcanic eruptions at different latitudes over the past millennium

Fei Liu[1*], Jinbao Li[2], Bin Wang[3], Jian Liu[4], Tim Li[3], Gang Huang[5] and Zhiyuan Wang[4]

[1]Earth System Modeling Center and Climate Dynamics Research Center, Nanjing University of Information Science and Technology, Nanjing, China

[2]Department of Geography, University of Hong Kong, Pokfulam, Hong Kong

[3]Department of Atmospheric Sciences and Atmosphere-Ocean Research Center, University of Hawaii at Manoa, Honolulu, HI 96825 USA

[4]Key Laboratory of Virtual Geographic Environment of Ministry of Education, School of Geography Science, Nanjing Normal University, Nanjing 210023, China

[5]State Key Laboratory of Numerical Modeling for Atmospheric Sciences and Geophysical Fluid Dynamics, Institute of Atmospheric Physics, Chinese Academy of Sciences, Beijing 100029, China

Submitted to *Climate Dynamics*

---

*To whom correspondence should be addressed. Dr. Fei Liu, Earth System Modeling Center, Nanjing University of Information Science and Technology, Nanjing, China

E-mail: liuf@nuist.edu.cn

Abstract

Detection and attribution of El Niño-Southern Oscillation (ENSO) responses to radiative forcing perturbation are critical for predicting the future change of ENSO under global warming. One of such forcing perturbation is the volcanic eruption. Our understanding of the responses of ENSO system to explosive tropical volcanic eruptions remains controversial, and we know little about the responses to high-latitude eruptions. Here, we synthesize proxy-based ENSO reconstructions, to show that there exist an El Niño-like response to the Northern Hemisphere (NH) and tropical eruptions and a La Niña-like response to the Southern Hemisphere (SH) eruptions over the past millennium. Our climate model simulation results show good agreement with the proxy records. The simulation reveals that due to different meridional thermal contrasts, the westerly wind anomalies can be excited over the tropical Pacific to the south of, at, or to the north of the equator in the first boreal winter after the NH, tropical, or SH eruptions, respectively. Thus, the eastern-Pacific El Niño can develop and peak in the second winter after the NH and tropical eruptions via the Bjerknes feedback. The model simulation only shows a central-Pacific El Niño-like response to the SH eruptions. The reason is that the anticyclonic wind anomaly associated with the SH eruption-induced southeast Pacific cooling will excite westward current anomalies and prevent the development of eastern-Pacific El Niño-like anomaly. These divergent responses to eruptions at different latitudes and in different hemispheres underline the sensitivity of the ENSO system to the spatial structure of radiative disturbances in the atmosphere.

Keywords: divergent El Niño responses; Northern Hemisphere volcanic eruptions;

Southern Hemisphere volcanic eruptions; ENSO; tree ring; reconstruction

1. Introduction

The El Niño-Southern Oscillation (ENSO) is a significant source of climate variability with global impacts (Deser et al. 2010). Understanding ENSO dynamics is of utmost importance to our society (McPhaden and Glantz 2007; Guilyardi et al. 2009; Collins et al. 2010). Effects of strong tropical volcanoes on the ENSO system have been demonstrated by both observations and model simulations (Handler 1984; Robock 2000; Adams et al. 2003; Mann et al. 2005; D'Arrigo et al. 2009; McGregor et al. 2010; Li et al. 2013; Ohba et al. 2013; Maher et al. 2015; Pausata et al. 2015), although controversy exists (Self et al. 1997; McGregor and Timmermann 2011; Zanchettin et al. 2012). The likelihood of El Niño is likely to increase after an explosive tropical volcanic eruption (Adams et al. 2003; McGregor et al. 2010; Li et al. 2013).

In model simulations, El Niño-like responses can be excited by tropical eruptions (Mann et al. 2005; Ohba et al. 2013; Maher et al. 2015; Predybaylo et al. 2017; Stevenson et al. 2017), and the main mechanism is the reduced role of the mean subsurface upwelling (Mann et al. 2005; Ohba et al. 2013; Maher et al. 2015), known as the dynamical thermostat mechanism, which is denoted by less cooling in the eastern equatorial Pacific than in the western equatorial Pacific (Seager et al. 1988; Clement et al. 1996). After a tropical eruption, the El Niño is also considered to be excited by the westerly anomalies induced by rapid surface cooling around the Maritime Continent

(Ohba et al. 2013). The process of less evaporation in the subtropical cloudless region by the cooling due to the eruptions also tends to weaken the intertropical convergence zone (ITCZ) and shift it equatorward (Lim et al. 2016). The equatorward migration of the ITCZ will reduce the easterly wind along the equator and excite an El Niño through the Bjerknes feedback (Bjerknes 1969).

The effect of asymmetric forcing associated to high-latitude volcanic eruptions on ENSO has generated growing attention recently (Pausata et al. 2015; Colose et al. 2016; Liu et al. 2016; Pausata et al. 2016; Stevenson et al. 2016). Although there are fewer studies on the Northern Hemisphere (NH) eruptions than on the tropical eruptions, the mechanism seems to be quite clear for these NH eruption-forced responses. After a volcanic eruption in the NH, an El Niño-like response is simulated (Pausata et al. 2015; Pausata et al. 2016; Stevenson et al. 2016). The consequent asymmetric cooling after a NH eruption will trigger the equatorial migration of the ITCZ (Colose et al. 2016; Stevenson et al. 2016), and the weakening of the easterly wind along the equator in the central-to-eastern Pacific will excite an El Niño through the Bjerknes feedback (Bjerknes 1969).

Based on the simulation of the Community Earth System Model (CESM) Last Millennium Ensemble (CESM-LME) (Stevenson et al. 2016), both tropical and NH eruptions are found to increase the probability of El Niño occurrences after the eruptions, especially in the second boreal winter after the eruptions. However, El Niño responses are not clear after the SH eruptions. It is unclear whether there are divergent ENSO responses to the NH, the tropical, and the SH eruptions in the reconstructions,

and if there are, what cause such differences. Previous study has shown that understanding of event-to-event differences in ENSO spatial pattern and evolution is important to improve the determination of ENSO prediction (Capotondi et al. 2015). Thus, in this study we aim to address these questions by synthesizing proxy-based ENSO reconstructions and climate model simulation.

2. Data and Methods

We analyze the newest dataset of millennium volcano reconstruction for the period of 500 BC to 2000 AD (Sigl et al. 2015) and 10 reconstructed ENSO indices (Stahle et al. 1998; Mann et al. 2000; D'Arrigo et al. 2005; Cook et al. 2008; Braganza et al. 2009; McGregor et al. 2010; Wilson et al. 2010; Li et al. 2011; Emile-Geay et al. 2013; Li et al. 2013). The instrumental sea surface temperature (SST) data from the Hadley Centre Ice and SST version 1 (HadISST1) are also used as a reference (Rayner et al. 2003). The NINO3 index in the instrumental observation and model simulations is calculated as the area averaged (150°W-90°W, 5°S-5°N) SST anomaly. Time series of all instrumental and reconstructed ENSO indices go through a 9-year Lanczos high-pass filter (Duchon 1979) to obtain the ENSO signal with a period of 2-8 years (D'Arrigo et al. 2005; Deser et al. 2010). All the time series are then normalized by their own standard deviations.

To explain the observed ENSO responses, a millennium volcanic sensitivity experiment is performed by running the CESM version 1.0 (CESM1) (Hurrell et al.

2013). A 2000-year control simulation is performed as the reference. To perform this control run, all external forcing is kept fixed at year-1850's values (Rosenbloom et al. 2013). Based on this control run, a millennium forced simulation is run for the period of 501 to 2000 AD, and all the external forcing is the same as that used in the control run except that the reconstruction of volcanic aerosols from 501 to 2000 AD is used as a variable forcing (Gao et al. 2008). A coarse resolution of T31 is used for both the control and sensitivity experiments. Compared to other models that participate in the fifth Coupled Models Intercomparison Project (CMIP5), the CESM has a good simulation of ENSO in terms of seasonality, amplitude, frequency, and associated teleconnection (Bellenger et al. 2014).

To identify climate responses to different volcanic eruptions, we use the superposed epoch analysis (SEA) (Haurwitz and Brier 1981). A window with seven years before and eight years after each eruption is used for the composite. The significance is calculated by the bootstrapped resampling method, and we repeat the SEA 10,000 times by using random draws from this study period. Following the work of Adams et al. (2003), each window is normalized by its maximum absolute anomaly to avoid one single large eruption dominating the composite.

3. Reconstructed ENSO proxies and volcanic forcing

Since the reconstructed ENSO proxies have notable discrepancies, we examine 10 conventional reconstructions of cold-season (namely, the boreal winter) ENSO indices

that cover various periods in the past millennium (Fig. 1), with the longest extending from 900 to 2002 AD (Li et al. 2011) and the shortest from 1706 to 1997 AD (Stahle et al. 1998). The number of records decreases as time goes back, and there are only two datasets containing information before 1300 AD. Since the longest reconstruction that has the largest weight in the composite analysis is obtained from the southwest North American tree rings (Li et al. 2011), we classify these reconstructions into two groups based on the regions the proxies are obtained. The first group is composed of reconstructions merely using the southwest North American tree rings, while the second group includes those developed from other global proxy records (Fig. 1). For each group, an ensemble mean for each year is calculated with available records. In this study, El Niño year is defined as the beginning year of the cold season, such as the strong El Niños occurred in 1982, 1991, and 1997. The 10 reconstructions are highly correlated with October-March instrumental NINO3 index using the HadISST1, with the correlations ranging from 0.53 to 0.95 for the period of 1871-2000, and the correlation between the mean of the 10 reconstructions and the instrumental NINO3 index is 0.87.

A large volcanic eruption can inject a large amount of sulphur dioxide into the stratosphere, which is then transformed into sulfuric acid aerosols, and the resulting aerosols perturb the climate through changing the radiation balance (Robock 2000). In this study, the following two sets of volcanic forcing will be used.

To analyze the responses of reconstructed ENSO to volcanic eruptions, we use the newest volcanic forcing during the past 2500 years (Sigl et al. 2015), which is obtained from the newest records of Greenland and Antarctic ice cores and age markers. During

the last millennium from 900 to 2000 AD when both ENSO and volcanic records are available, there were 131 strong eruptions (Fig. 2a).

To perform the millennium volcanic sensitivity experiments, we use the 1500-year volcanic reconstruction of Gao et al. (2008), which has been used in the Paleoclimate Modeling Intercomparison Project 3 (PMIP3). For each eruption, the aerosol density reaches maximum in the fifth month after the eruption and decays quickly to recover to the background state within two years (Liu et al. 2016). Thus, the year is defined as the eruption year when its annual aerosol is larger than the two years before and after it. When the eruption starts late in the year, e.g., November or December, it has maximum aerosol density in the following year; in such case, the following year is considered as the eruption year when analyzing the numerical experiment outputs.

In the sensitivity simulation carried out in this study, we only consider the strong eruptions with annual aerosol amount above 48 Tg, which is the average aerosol mass in the eruption years for all eruptions during the last 1500 years. Thus, during the simulated 1500 years, there were 54 explosive volcanoes (Fig. 2a). Previous study showed that there is a threshold of volcano strength above which the volcanic forcing can excite El Niño-like responses (Lim et al. 2016). In our study, only strong eruptions are studied, and this threshold of volcano strength is not discussed. Compared to the study based on the CESM-LME with more members (Stevenson et al. 2016), only one millennium member is run here; thus, we need more eruption samples to remove the internal interannual variability in the SEA analysis.

When analyzing the ENSO responses, we classify eruptions into three groups, i.e.,

177 the NH, SH, or tropical eruptions. For both datasets, the classification is based on the
178 sulfate deposition in the ice sheets of two polar regions. In the dataset of Sigl et al.
179 (2015), these three groups have already been separated by comparing sulfate
180 depositions on both polar ice sheets. During the period from 900 to 2000 AD, there
181 were 66 NH, 26 SH, and 39 tropical eruptions. In the dataset of Gao et al. (2008), the
182 meridional aerosol distribution for each eruption is well defined (Fig. 2b). One group
183 has sulfate depositions in both polar ice sheets, while the other two groups only have
184 sulfate deposition in one of these two polar regions. Based on the classification defined
185 by Liu et al. (2016), we define an eruption as a NH event if the volcanic aerosol burden
186 is zero at 40^{o}S, as a SH event if the volcanic aerosol burden is zero at 40^{o}N, and as a
187 tropical event if the volcanic aerosol burden is above zero at both 40^{o}S and 40^{o}N. Thus,
188 the NH, the tropical, and the SH eruptions have their aerosols centered in the NH, the
189 tropics, and the SH, respectively (Fig. 2b). During the simulated 1500 years from 501
190 to 2000 AD, there were 16 NH, 25 tropical, and 13 SH explosive volcanoes. When
191 using the definition based on the aerosols' concentration difference between
192 hemispheres, the meridional asymmetry of the tropical eruptions is weak (Colose et al.
193 2016; Stevenson et al. 2016). The tropical eruptions obtained based on our definition
194 have a somewhat larger meridional asymmetry (Fig. 2b). Since tropical eruptions are
195 not always symmetric (Toohey et al. 2011), a threshold of meridional distribution of
196 these tropical eruptions, which leads to different tropical responses, is worth analyzing
197 in the future.
198

4. Proxy-based ENSO after different volcanic eruptions

To analyze the responses of ENSO system to different volcanic eruptions, we perform SEA on the ensemble mean of the 10 ENSO reconstructions during 900-2000 AD (Fig. 3). The results indicate that significant El Niño-like responses occur one year following the NH eruptions and in the same year of the tropical eruptions. For the SH eruptions, however, no El Niño-like composite response is found. Instead, a La Niña-like response happens within three years after the SH eruptions. Interestingly, a strong La Niña-like response to the tropical eruptions can be observed two years after the tropical eruptions (+2), and a La Niña-like response to the NH eruptions is also observed three years after the NH eruptions (+3). These La Niña-like responses were also noted by other researchers (Li et al. 2013; Maher et al. 2015; Pausata et al. 2015). Although it is argued that this transition to La Niña-like responses is dynamically driven rather than a consequence of the general post-eruption cooling (Pausata et al. 2016), the underlying mechanism for these quick transitions from eruption-induced El Niño to La Niña needs further investigation.

The above results show clear divergent responses of the proxy ENSO indices to the NH, the tropical, and the SH eruptions during the past millennium. Such divergent responses are most evident in ENSO reconstructions based on the North American tree rings, but less clear in those reconstructions based on global proxy records (Fig. 3). For each eruption, when all available ENSO reconstructions instead of their mean are used for the SEA analysis, similar divergent responses are also identified (Fig. 4). For the 10 reconstructions, the divergent responses are much clearer in the three reconstructions

based on the North American tree rings than in the seven reconstructions based on global proxy records (Fig. 5). One hypothesis for the different responses is that the ENSO teleconnection in some regions was not stable during the last millennium (Li et al. 2013), and the inclusion of proxy records from regions with unstable teleconnections may damp the ENSO signal. To confirm this hypothesis, more analysis on ENSO-related global teleconnection in different warm and cold epochs of the last millennium is necessary by using millennium simulations in the future.

To confirm the divergent responses, we use the mean of the three ENSO indices based on the North American tree rings. An increase of two-year (0 and +1) mean ENSO index occurs for 40 out of the 66 (61%) NH eruptions and for 27 out of the 39 (69%) tropical eruptions, compared to the pre-eruption seven-year (-7 and -1) mean. A decrease of two-year mean ENSO index, however, occurs for 17 out of the 26 (65%) SH eruptions. Before each SH eruption, the negative ENSO index is also counted and a decrease occurs for 19 out of the 26 (73%) for the year -4 compared to the pre-eruption seven-year mean. These results are consistent with the SEA analysis results (Fig. 3). In the SEA on the reconstructions, some significant NINO3 responses are seen before the eruptions (Fig. 3), which seems to suggest that the SEA has some uncertainties when separating the internal and external forcing-induced modes in the reconstructions. For the internal mode without any external forcing, the interannual variability can be largely removed by SEA analysis. This is supported by performing SEA analysis on 30 random non-volcanic event “windows”, and the results shows no significant responses (figure not shown). Thus, the significant responses before the eruptions may also be attributed

to the uncertainty of the reconstructions rather than to the SEA analysis itself.

5. Simulated ENSO after different volcanic eruptions

To confirm and understand these divergent ENSO responses to the NH, the tropical, and the SH eruptions, we perform a millennium volcanic sensitivity experiment using CESM1 for the period of 501-2000 AD. In this millennium simulation, volcanic forcing is the only external forcing allowed to change over time, which is derived from version 1 of the ice-core dataset based reconstruction by Gao et al. (2008). In this dataset, most of the eruptions are assumed to occur in April. So, the effect of eruption season, which is found to excite different eruption-year circulations (Stevenson et al. 2017), cannot be considered here. Compared to the 2000-year control run that has an ENSO amplitude of 0.85^{o}C, defined by the standard deviation of the boreal winter (December-February) NINO3 index, the 1500-year volcanic sensitivity experiment has somewhat larger ENSO amplitude of 0.87^{o}C.

After the NH eruptions (Fig. 6a), the simulated NINO3 index is weakly negative in the year (0), and it becomes positive after the spring of year (+1) and reaches a maximum in that winter. In year (+2), the Niño3 index decreases quickly with a minimum occurring in that winter (Fig. 6b). Similar results are seen after the tropical eruptions, except for stronger negative NINO3 index simulated in year (0) and year (+2). For the SH eruptions, a negative NINO3 index is also simulated in year (0) and year (+2), but the positive NINO3 index in year (1) is weak and reaches a maximum in

265 the summer of that year and decreases quickly thereafter.

266 After the NH or tropical eruptions (Fig. 6c), positive SST anomalies occur in the
267 eastern Pacific in the spring of year (+1), and then develop and propagate westward
268 into the central-eastern Pacific in winter. After the SH eruptions, warm SST begins in
269 the western Pacific in the spring of year (+1), and then propagates eastward. This warm
270 SST, however, cannot develop over the eastern Pacific in the winter one year after the
271 SH eruptions.

272 Due to direct reduction of shortwave radiation caused by eruptions at different
273 latitudes, global circulation and precipitation have different responses in the winter of
274 the eruption year (0) (Fig. 7). Following the NH eruptions, a significant precipitation
275 decrease is seen over a great part of the NH; in particular, the model simulates an
276 equatorial migration of the ITCZ (Fig. 7a), which is consistent with previous studies
277 (Pausata et al. 2015; Colose et al. 2016; Stevenson et al. 2016). The increase of
278 precipitation occurs over the south part of the equatorial regions in the Indo-Pacific and
279 Atlantic (Fig. 7a). Thus, marked westerly wind anomalies are excited over the central-
280 to-eastern Pacific to the south of the equator.

281 After the tropical eruptions (Fig. 7b), significant precipitation decrease occurs over
282 the tropical regions, including the equatorial Indo-western Pacific, the Pacific ITCZ,
283 and the South Pacific Convergence Zone (SPCZ) regions, while large precipitation
284 increase happens over the subtropical regions and small increase occurs over the
285 central-to-eastern equatorial Pacific. Thus, significant westerly wind anomalies are
286 excited over the equatorial Pacific because of the divergence over the Indo-western

Pacific. Over the off-equatorial region in the tropical Pacific, the westerly wind anomalies can also be excited by the weakening of the ITCZ and SPCZ through the quasi-geostrophic balance.

After the SH eruptions (Fig. 7c), significant precipitation decrease is simulated in the SH, especially in the south Maritime Continent, Australian monsoon region, and the central Pacific south of the equator. Large precipitation increase occurs from the western North Pacific to the central Pacific north of the equator. Thus, significant westerly wind anomalies are excited from the western-to-central Pacific to the north of the equator.

Since the stratospheric aerosols associated with the NH eruptions are concentrated in the NH, the surface cooling mainly happens in the NH, while the SH is less affected (Fig. 8a); thus, the lower-tropospheric moisture is much reduced in the NH region, with maximum decrease at 6^{o}N. This southward surface temperature gradient also induces significant downward motion and divergence near 10^{o}N. The moisture convergence anomalies, consistent with precipitation anomalies (figure not shown), are mainly induced by the circulation change (Fig. 8b), which means the equatorward migration of the ITCZ is mainly caused by the circulation change induced by the NH cooling and associated southward temperature gradient. In other words, the interhemispheric thermal contrast after the NH eruptions pushes the ITCZ away from the hemisphere that is cooled (Kang et al. 2008; Schneider et al. 2014; Pausata et al. 2015; Stevenson et al. 2016).

After the tropical eruptions, because of the strong aerosol concentration at the low

309 latitude, the surface temperature in the tropics is significant decreased (Fig. 9a),
310 resulting in large moisture decrease in the tropics. In this study, the tropical eruptions
311 also have somewhat larger aerosol density in the NH than in the SH, which results in
312 larger temperature decrease in the NH than in the SH; thus, significant divergence also
313 occurs to the north of the equator. Because of the large moisture decrease in the tropics,
314 moisture convergence and precipitation decrease occur in the tropics (Fig. 9b). The
315 circulation change, i.e., the divergence to the north of the equator, also induces
316 additional precipitation decrease in the ITCZ. With the same mechanism for the
317 weakening of the ITCZ induced by the NH eruptions (Fig. 8), the strong precipitation
318 decrease in the SH after the SH eruptions is mainly caused by the circulation change
319 induced by the northward surface temperature gradient (Fig. 10).

320 After the NH eruptions (Fig. 11a), the westerly wind anomalies are excited to the
321 south of the equator over the Pacific in the first boreal winter, and warm SSTs begin to
322 develop from the eastern Pacific after the spring associated with this westerly wind
323 anomalies via the Bjerknes feedback. The warm SSTs also begin to develop in the
324 eastern Pacific associated with the equatorial westerly wind anomalies since the first
325 boreal winter after the tropical eruptions (Fig. 11b). After the SH eruptions (Fig. 11c),
326 the southeastern Pacific is always dominated by the anticyclonic wind anomalies
327 associated with cold SST anomalies. Compared to the westerly wind anomalies and
328 their associated downwelling in the central-to-eastern Pacific in the summer one year
329 after the NH or the tropical eruptions, the easterly wind anomalies and the associated
330 upwelling dominate the eastern Pacific in the summer one year after the SH eruptions

(Fig. 12). Thus, this upwelling prevents warm SST anomalies from developing in the eastern Pacific, again via the Bjerknes feedback.

Compared to the internal El Niño in the control run (Fig. 13), the transition from El Niño to La Niña is much faster for the tropical eruption-induced El Niño. The negative NINO3 index appears early in May for this forced El Niño, which only occurs in July for the internal mode in the control run. The La Niña after the El Niño for the eruption-forced mode is also stronger than that for the internal mode. The easterly wind anomaly over the western Pacific appears in May after the El Niño for the internal mode, while it appears early in January and is very strong for the forced mode. Since the volcanic forcing is very weak during this El Niño-La Niña transition year, i.e., the second year after the eruptions (Fig. 6), this fast transition after the tropical eruption-induced El Niño is dynamically driven, i.e., it is caused by the strong easterly wind anomaly rather than by the cooling. The underlying mechanism for the formation of the easterly wind anomaly needs further investigation.

6. Concluding remarks

In summary, by using the newest volcanic forcing records and 10 reconstructed ENSO indices, we show that the tropical and NH eruptions can trigger an El Niño-like event within two years after the eruptions. These El Niño-like responses, however, are not found after the SH eruptions. Instead, a weak La Niña-like event tends to occur within three years after the SH eruptions. These divergent responses of ENSO to the

NH, the tropical, and the SH volcanic eruptions are simulated by the millennium volcanic sensitivity experiment. The El Niño-like responses are simulated in the winter one year after the NH or tropical eruptions, while the El Niño-like response cannot develop in the winter after the SH eruptions. The mechanisms for these divergent ENSO responses are summarized in Fig. 14. Due to different interhemispheric thermal contrast or high latitude-tropical thermal contrast caused by the volcanic cooling, precipitation decrease mainly occurs to the north of, at, and to the south of the equator in the first winter after the NH, tropical, or SH eruptions; thus, the westerly wind anomalies are excited over the tropical Pacific to the south of, at, or to the north of the equator accordingly. The El Niño can develop and peak in the second winter after the NH or tropical eruptions through the Bjerknes feedback. After the SH eruptions, however, the volcano-induced southeast Pacific cooling will excite anticyclonic wind anomalies, which will induce strong westward current anomalies to prevent the warm SST from developing in the eastern Pacific. As a result, a central-Pacific El Niño-like response is obtained in the second winter after the SH eruptions.

Although previous study (Stevenson et al. 2016) and our own work all showed overly large model and proxy disagreement in eruption years, the eastern Pacific El Niño-like responses have been observed and simulated within two years after the NH or tropical eruptions. After the SH eruptions, the proxy shows occurrence of La Niña-like event, while the model simulation presents central-Pacific El Niño-like responses. This simulation of central-Pacific El Niño-like responses should improve our understanding of the central-Pacific El Niño that has been observed frequently in recent years (Ashok

et al. 2007; Ashok and Yamagata 2009); and it may also provide an explanation on the natural variations of the central-Pacific El Niño (Newman et al. 2011; Yeh et al. 2011). Both observations and simulations indicate that there are no eastern Pacific El Niño-like events after the SH eruptions, largely due to easterly wind anomalies that suppress the Bjerknes feedback in the eastern Pacific. Different ENSO responses to the NH, the tropical, and the SH eruptions provide us different angles to understand ENSO mechanisms.

The findings in this study are based on the SEA analysis. From a modeling perspective, ensemble simulations are the most suited method to study volcano-forced responses (Pausata et al. 2015; Pausata et al. 2016; Stevenson et al. 2017). In future, ensemble simulations should be used to study these divergent ENSO responses to different volcanos.

Acknowledgements. We thank Christopher M. Colose and two anonymous reviewers for their valuable comments and helpful suggestions. F.L. acknowledges the support from the National Natural Science Foundation of China (41420104002), the China National 973 Project (2015CB453200), and the Natural Science Foundation of Jiangsu (2015CB453200). J.B.L. acknowledges the support from the Hong Kong Research Grants Council (Project No. 27300514). B.W. acknowledges the support from the National Science Foundation of the US (climate dynamics division Award No. AGS-1540783) and the Global Research Laboratory (GRL) Program of the National

Research Foundation of Korea (Grant No. 2011-0021927). This paper is ESMC Contribution No. XXXX.

References

Adams JB, Mann ME, Ammann CM (2003) Proxy evidence for an El Nino-like response to volcanic forcing. Nature 426:274-278

Ashok K, Behera SK, Rao SA, Weng H, Yamagata T (2007) El Niño Modoki and its possible teleconnection. Journal of Geophysical Research (Oceans) 112:11007

Ashok K, Yamagata T (2009) Climate change: The El Niño with a difference. Nature 461:481-484

Bellenger H, Guilyardi E, Leloup J, Lengaigne M, Vialard J (2014) ENSO representation in climate models: from CMIP3 to CMIP5. Clim Dynam 42:1999-2018 doi:10.1007/s00382-013-1783-z

Bjerknes J (1969) Atmospheric teleconnections from the equatorial Pacific. Mon Weather Rev 97:163-172

Braganza K, Gergis JL, Power SB, Risbey JS, Fowler AM (2009) A multiproxy index of the El Nino–Southern Oscillation, AD 1525–1982. Journal of Geophysical Research: Atmospheres 114

Capotondi A et al. (2015) Understanding ENSO diversity. B Am Meteorol Soc 96:921-938

Clement AC, Seager R, Cane MA, Zebiak SE (1996) An ocean dynamical thermostat. J Climate 9:2190-2196

Collins M et al. (2010) The impact of global warming on the tropical Pacific Ocean and El Niño. Nature Geoscience 3:391-397

Colose CM, LeGrande AN, Vuille M (2016) Hemispherically asymmetric volcanic

441 forcing of tropical hydroclimate and water isotopologue variability during the
442 last millennium. Earth Syst Dynam Discuss 2016:1-52 doi:10.5194/esd-2016-
443 19
444 Cook E, D'Arrigo R, Anchukaitis K (2008) ENSO reconstructions from long tree-ring
445 chronologies: Unifying the differences? Talk presented at a special workshop
446 on "Reconciling ENSO Chronologies for the Past 500 Years", held in Moorea.
447 French Polynesia on April 2-3
448 D'Arrigo R, Cook ER, Wilson RJ, Allan R, Mann ME (2005) On the variability of
449 ENSO over the past six centuries. Geophys Res Lett 32
450 D'Arrigo R, Wilson R, Tudhope A (2009) The impact of volcanic forcing on tropical
451 temperatures during the past four centuries. Nature Geoscience 2:51-56
452 Deser C, Alexander MA, Xie SP, Phillips AS (2010) Sea surface temperature variability:
453 patterns and mechanisms. Annual Review of Marine Science 2:115-143
454 Duchon CE (1979) Lanczos filtering in one and two dimensions. J Appl Meteorol
455 18:1016-1022
456 Emile-Geay J, Cobb KM, Mann ME, Wittenberg AT (2013) Estimating central
457 equatorial Pacific SST variability over the past millennium. Part II:
458 Reconstructions and implications. J Climate 26:2329-2352
459 Gao C, Robock A, Ammann C (2008) Volcanic forcing of climate over the past 1500
460 years: An improved ice core-based index for climate models. Journal of
461 Geophysical Research: Atmospheres 113 doi:10.1029/2008JD010239
462 Guilyardi E et al. (2009) Understanding El Niño in ocean-atmosphere general

463 circulation models: progress and challenges. B Am Meteorol Soc 90:325-340
464 Handler P (1984) Possible association of stratospheric aerosols and El Nino type events.
465 Geophys Res Lett 11:1121-1124
466 Haurwitz MW, Brier GW (1981) A critique of the superposed epoch analysis method:
467 its application to solar-weather relations. Mon Weather Rev 109:2074-2079
468 Hurrell JW et al. (2013) The community earth system model: a framework for
469 collaborative research. B Am Meteorol Soc 94:1339-1360
470 Kang SM, Held IM, Frierson DM, Zhao M (2008) The response of the ITCZ to
471 extratropical thermal forcing: Idealized slab-ocean experiments with a GCM. J
472 Climate 21:3521-3532
473 Li J et al. (2011) Interdecadal modulation of El Niño amplitude during the past
474 millennium. Nature Climate Change 1:114-118
475 Li J et al. (2013) El Nino modulations over the past seven centuries. Nature Climate
476 Change 3:822-826
477 Lim HG, Yeh SW, Kug JS, Park YG, Park JH, Park R, Song CK (2016) Threshold of
478 the volcanic forcing that leads the El Niño-like warming in the last millennium:
479 results from the ERIK simulation. Clim Dynam 46:3725-3736
480 Liu F, Chai J, Wang B, Liu J, Zhang X, Wang Z (2016) Global monsoon precipitation
481 responses to large volcanic eruptions. Scientific Reports 6:24331
482 doi:10.1038/srep24331
483 Maher N, McGregor S, England MH, Gupta AS (2015) Effects of volcanism on tropical
484 variability. Geophys Res Lett 42:6024-6033 doi:10.1002/2015GL064751

485 Mann ME, Cane MA, Zebiak SE, Clement A (2005) Volcanic and solar forcing of the
486 tropical Pacific over the past 1000 years. J Climate 18(3):447-456
487 Mann ME, Gille E, Overpeck J, Gross W, Bradley RS, Keimig FT, Hughes MK (2000)
488 Global temperature patterns in past centuries: An interactive presentation. Earth
489 interactions 4:1-1
490 McGregor S, Timmermann A (2011) The effect of explosive tropical volcanism on
491 ENSO. J Climate 24:2178-2191
492 McGregor S, Timmermann A, Timm O (2010) A unified proxy for ENSO and PDO
493 variability since 1650. CliPa 6:1-17
494 McPhaden MJ, Glantz MH (2007) ENSO as an integrating concept in earth science.
495 Science 314:1740-1745
496 Newman M, Shin SI, Alexander MA (2011) Natural variation in ENSO flavors.
497 Geophys Res Lett 38
498 Ohba M, Shiogama H, Yokohata T, Watanabe M (2013) Impact of strong tropical
499 volcanic eruptions on ENSO simulated in a coupled GCM. J Climate 26:5169-
500 5182
501 Pausata FS, Chafik L, Caballero R, Battisti DS (2015) Impacts of high-latitude volcanic
502 eruptions on ENSO and AMOC. Proc Natl Acad Sci USA 112:13784-13788
503 Pausata FSR, Karamperidou C, Caballero R, Battisti DS (2016) ENSO response to
504 high‐latitude volcanic eruptions in the Northern Hemisphere: The role of the
505 initial conditions. Geophys Res Lett 43
506 Predybaylo E, Stenchikov GL, Wittenberg AT, Zeng F (2017) Impacts of a Pinatubo‐

507 Size Volcanic Eruption on ENSO. Journal of Geophysical Research:
508 Atmospheres
509 Rayner N et al. (2003) Global analyses of sea surface temperature, sea ice, and night
510 marine air temperature since the late nineteenth century. Journal of Geophysical
511 Research: Atmospheres (1984–2012) 108:4407
512 Robock A (2000) Volcanic eruptions and climate. Rev Geophys 38:191-219
513 Rosenbloom N, Otto-Bliesner B, Brady E, Lawrence P (2013) Simulating the mid-
514 Pliocene Warm Period with the CCSM4 model. Geoscientific Model
515 Development 6:549-561
516 Schneider T, Bischoff T, Haug GH (2014) Migrations and dynamics of the intertropical
517 convergence zone. Nature 513:45-53
518 Seager R, Zebiak SE, Cane MA (1988) A model of the tropical Pacific sea surface
519 temperature climatology. Journal of Geophysical Research Atmospheres
520 93:1265–1280
521 Self S, Rampino M, Zhao J, Katz M (1997) Volcanic aerosol perturbations and strong
522 El Nino events: No general correlation. Geophys Res Lett 24:1247-1250
523 Sigl M et al. (2015) Timing and climate forcing of volcanic eruptions for the past 2,500
524 years. Nature 523:543-549 doi:10.1038/nature14565
525 Stahle DW, D'Arrigo RD, Krusic PJ, Cleaveland MK (1998) Experimental
526 dendroclimatic reconstruction of the Southern Oscillation. B Am Meteorol Soc
527 79:2137
528 Stevenson S, Fasullo JT, Ottobliesner BL, Tomas RA, Gao C (2017) Role of eruption

529 season in reconciling model and proxy responses to tropical volcanism.
530 Proceedings of the National Academy of Sciences of the United States of
531 America 114:1822
532 Stevenson S, Otto-Bliesner B, Fasullo J, Brady E (2016) “El Niño Like” Hydroclimate
533 Responses to Last Millennium Volcanic Eruptions. J Climate 29:2907-2921
534 Toohey M, Krüger K, Niemeier U, Timmreck C (2011) The influence of eruption season
535 on the global aerosol evolution and radiative impact of tropical volcanic
536 eruptions. ACP 11:22443-22481
537 Wilson R, Cook E, D'Arrigo R, Riedwyl N, Evans MN, Tudhope A, Allan R (2010)
538 Reconstructing ENSO: the influence of method, proxy data, climate forcing and
539 teleconnections. J Quaternary Sci 25:62-78
540 Yeh SW, Kirtman BP, Kug JS, Park W, Latif M (2011) Natural variability of the central
541 Pacific El Niño event on multi‐centennial timescales. Geophys Res Lett 38
542 Zanchettin D et al. (2012) Bi-decadal variability excited in the coupled ocean–
543 atmosphere system by strong tropical volcanic eruptions. Clim Dynam 39:419-
544 444
545
546
547
548
549
550

551 **List of Figures**

552 **Fig. 1** Long-term ENSO reconstructions. Shown are the instrumental (Rayner et al.
553 2003) October-March NINO3 index (red line), 10 different ENSO reconstructions (gray
554 lines) (Stahle et al. 1998; Mann et al. 2000; D'Arrigo et al. 2005; Cook et al. 2008;
555 Braganza et al. 2009; McGregor et al. 2010; Wilson et al. 2010; Li et al. 2011; Emile-
556 Geay et al. 2013; Li et al. 2013), and the mean of these reconstructions (dark gray line).
557 The inset shows the period 1871-2000. All records were processed using a 9-year
558 Lanczos high-pass filter. The three available reconstructions based on the North
559 American tree rings and seven reconstructions based on global proxies are shown by
560 green and brown shading, respectively. Triangles and dotted vertical lines denote cold
561 seasons (defined by the beginning year of the cold season of the NH) following the NH
562 (red), the tropical (dark), and the SH (blue) eruptions back to 900 AD.

563 **Fig. 2** Reconstructed volcanic forcing. **a** Shown are the global average, annual-mean
564 volcanic aerosols for 16 NH (red), 13 SH (blue), and 25 tropical (green) strong
565 eruptions from 500 to 2000 AD reconstructed by Gao et al. (2008); and for 66 NH, 26
566 SH, and 39 tropical volcanic eruptions from 900 to 2000 AD reconstructed by Sigl et
567 al. (2015). **b** Meridional distribution of zonally-averaged, annual-mean aerosols column
568 density (thin lines) for these 16 NH, 13 SH, and 25 tropical strong eruptions from 500
569 to 2000 AD reconstructed by Gao et al. (2008). The thick lines denote the averaged
570 profiles for these NH, SH, and tropical eruptions. Adapted from Liu et al. (2016).

571 **Fig. 3** Reconstructed cold-season ENSO SEA results. Normalized results for responses
572 of the mean of the 10 reconstructions to the NH (**a**), the tropical (**b**), and the SH (**c**)

eruptions are shown (upper panels) for the period 900-2000 AD. Confidence limits (90%, 95%, 99%) are marked by horizontal lines. Blue and red colors mark the pre-eruption and post-eruption composites, respectively. The number in each panel denotes the eruption event number. "0" denotes the first cold season following the eruptions. All records were processed using a 9-year Lanczos high-pass filter. The SEA results are also shown for the mean of the three reconstructions based on the North American tree rings from 900 to 2000 AD (middle panels) and for the seven reconstructions based on global proxies from 1149 to 2000 AD (bottom panels).

Fig. 4 Reconstructed cold-season ENSO SEA results. Same as Fig. 3, except that for each eruption, all available reconstructions are used for its composite using the same weight, and the number in each panel denotes the composite number.

Fig. 5 Reconstructed cold-season ENSO SEA results for each reconstruction. Same as Fig. 3, except for each of the 10 reconstructions, and the number in each panel denotes the composite number.

Fig. 6 Model responses to different volcanic eruptions. Zonally-averaged aerosol column density (**a**), normalized SEA results of NINO3 index (**b**), and equatorial (5^{o}S-5^{o}N average) SST anomalies (**c**) are shown for 16 NH eruptions (left panels), 25 tropical eruptions (middle panels), and 13 SH eruptions (right panels). Confidence limits (90%, 95%, 99%) are marked by horizontal lines for composite NINO3, and the equatorial SST anomalies significant above the 95% confidence level are marked by stippling. Blue and red bars mark the pre- and post-eruption years, respectively. "0" denotes the year of each eruption, and "+1" indicates one year after the eruption.

595 **Fig. 7** Spatial patterns of different volcano-forced modes. The normalized composite
596 precipitation (shading) and 850-hPa wind (vectors) anomalies are shown for the first
597 winter (December-February) after the NH (**a**), the tropical (**b**), and the SH (**c**) eruptions.
598 Stippling indicates the >95% confidence level based on the Monte Carlo resampling
599 (n=10,000). Only the wind anomalies above the 95% significance level are drawn.
600 **Fig. 8** Meridional distributions of NH volcano-induced responses. The normalized
601 composite zonal-mean anomalies of (**a**) surface temperature (dark line), 500-hPa
602 vertical velocity (w', red line) and 850-hPa specific humidity (q', blue line), and (**b**)
603 total moisture convergence (w'q+wq', dark line), circulation change-induced moisture
604 convergence (w'q, red line), and moisture change-induced moisture convergence (wq',
605 blue line) are shown for the first winter (December-February) after the NH eruptions.
606 Prime denotes the anomaly, and anomalies above the 95% significance level are shown
607 by solid lines.
608 **Fig. 9** Same as Fig. 8, except for the tropical eruptions.
609 **Fig. 10** Same as Fig. 8, except for the SH eruptions.
610 **Fig. 11** SST anomaly evolutions after different eruptions. The composites of normalized
611 three-month-mean SST anomalies (shading) and 850-hPa wind anomalies (vectors)
612 since the first winter after the NH (**a**), the tropical (**b**), and the SH (**c**) eruptions. "0"
613 denotes the year of each eruption, and "+1" indicates one year after the eruption.
614 **Fig. 12** Different oceanic responses to different eruptions. The normalized composite
615 summer-mean (June-August) surface currents and surface (0-20 m) upwelling
616 anomalies one year after the NH (**a**), the tropical (**b**), and the SH (**c**) eruptions.

Fig. 13 Transition to La Niña from tropical eruption-induced El Niño mode and internal El Niño mode. Shown are the composite NINO3 index for 25 tropical eruptions (thick red line) and for the El Niño in the control run (thick blue line), as well as the associated zonal wind anomalies (dashed lines) averaged over the western Pacific (5^oS-5^oN, 120^oE-150^oE). "1" denotes one year after each eruption, and "2", two years. The El Niño in the control run is defined when the boreal winter (December-February average) NINO index is above one standard deviation. Each variable is normalized by its maximum value in years "1" and "2".

Fig. 14 Schematic diagram showing different eruption-induced responses. Shown are surface cooling (blue shading), precipitation anomaly (cloud), and surface wind anomaly (vector) in the first boreal winter after the NH eruptions (**a**), the tropical eruptions (**b**), and the SH eruptions (**c**). Positive/negative precipitation anomaly is denoted by green/brown cloud. The blue ellipse denotes the southeast Pacific cooling.

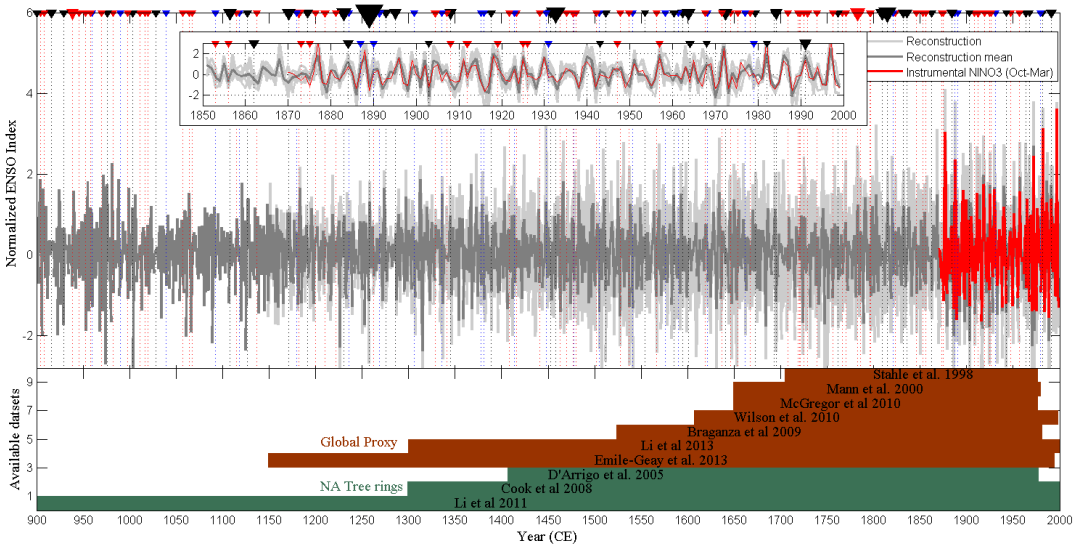

Fig. 1 Long-term ENSO reconstructions. Shown are the instrumental (Rayner et al. 2003) October-March NINO3 index (red line), 10 different ENSO reconstructions (gray lines) (Stahle et al. 1998; Mann et al. 2000; D'Arrigo et al. 2005; Cook et al. 2008; Braganza et al. 2009; McGregor et al. 2010; Wilson et al. 2010; Li et al. 2011; Emile-Geay et al. 2013; Li et al. 2013), and the mean of these reconstructions (dark gray line). The inset shows the period 1871-2000. All records were processed using a 9-year Lanczos high-pass filter. The three available reconstructions based on the North American tree rings and seven reconstructions based on global proxies are shown by green and brown shading, respectively. Triangles and dotted vertical lines denote cold seasons (defined by the beginning year of the cold season of the NH) following the NH (red), the tropical (dark), and the SH (blue) eruptions back to 900 AD.

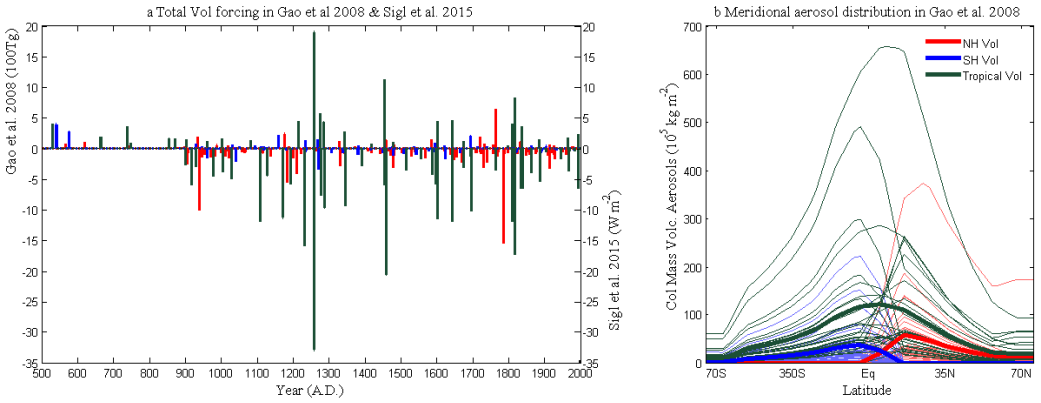

Fig. 2 Reconstructed volcanic forcing. **a** Shown are the global average, annual-mean volcanic aerosols for 16 NH (red), 13 SH (blue), and 25 tropical (green) strong eruptions from 500 to 2000 AD reconstructed by Gao et al. (2008); and for 66 NH, 26 SH, and 39 tropical volcanic eruptions from 900 to 2000 AD reconstructed by Sigl et al. (2015). **b** Meridional distribution of zonally-averaged, annual-mean aerosols column density (thin lines) for these 16 NH, 13 SH, and 25 tropical strong eruptions from 500 to 2000 AD reconstructed by Gao et al. (2008). The thick lines denote the averaged profiles for these NH, SH, and tropical eruptions. Adapted from Liu et al. (2016).

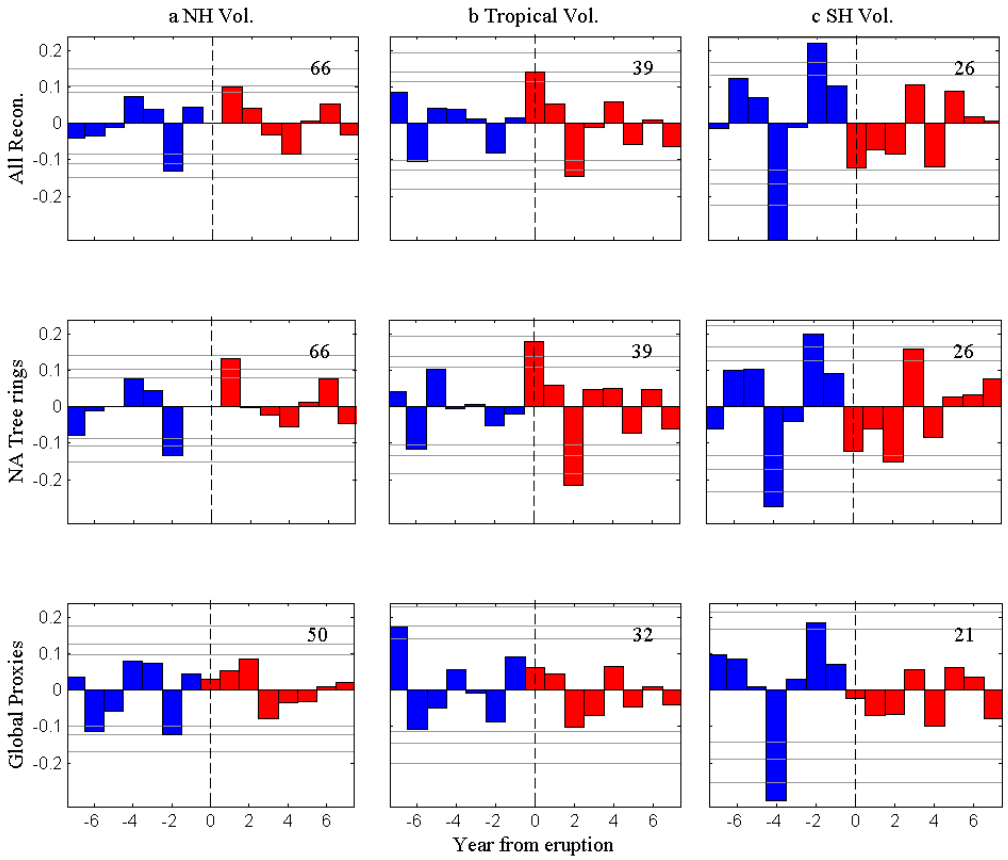

Fig. 3 Reconstructed cold-season ENSO SEA results. Normalized results for responses of the mean of the 10 reconstructions to the NH (**a**), the tropical (**b**), and the SH (**c**) eruptions are shown (upper panels) for the period 900-2000 AD. Confidence limits (90%, 95%, 99%) are marked by horizontal lines. Blue and red colors mark the pre-eruption and post-eruption composites, respectively. The number in each panel denotes the eruption event number. "0" denotes the first cold season following the eruptions. All records were processed using a 9-year Lanczos high-pass filter. The SEA results are also shown for the mean of the three reconstructions based on the North American tree rings from 900 to 2000 AD (middle panels) and for the seven reconstructions based on global proxies from 1149 to 2000 AD (bottom panels).

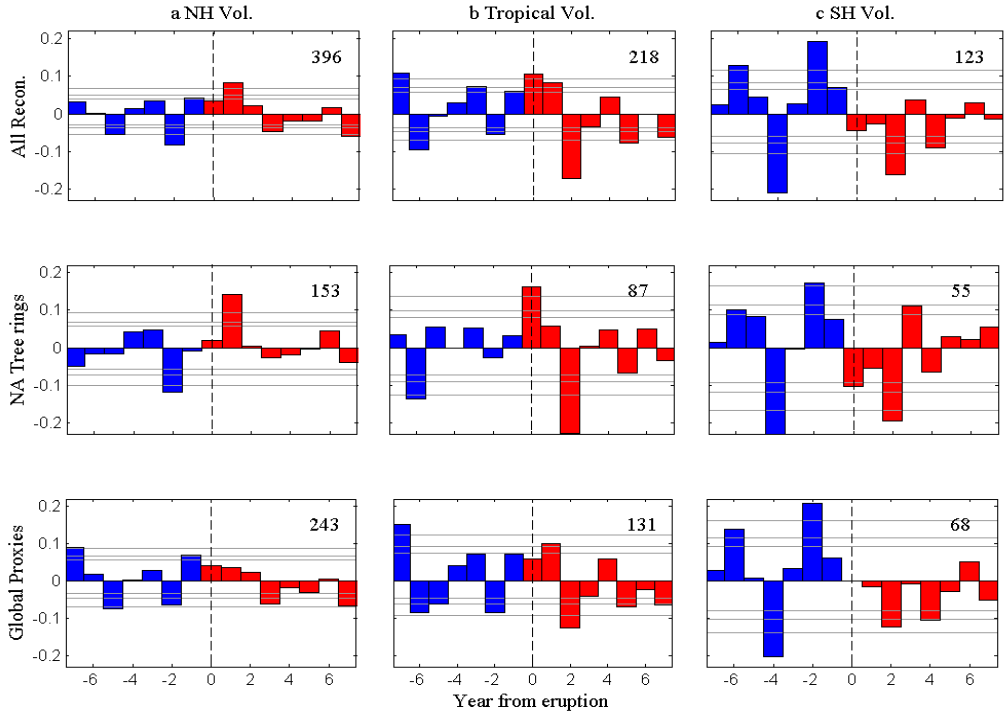

677

678 **Fig. 4** Reconstructed cold-season ENSO SEA results. Same as Fig. 3, except that for

679 each eruption, all available reconstructions are used for its composite using the same

680 weight, and the number in each panel denotes the composite number.

681

682

683

684

685

686

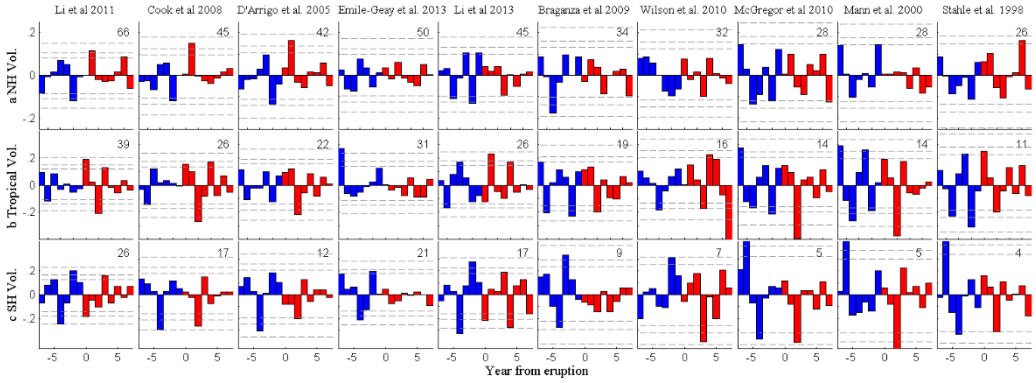

Fig. 5 Reconstructed cold-season ENSO SEA results for each reconstruction. Same as Fig. 3, except for each of the 10 reconstructions, and the number in each panel denotes the composite number.

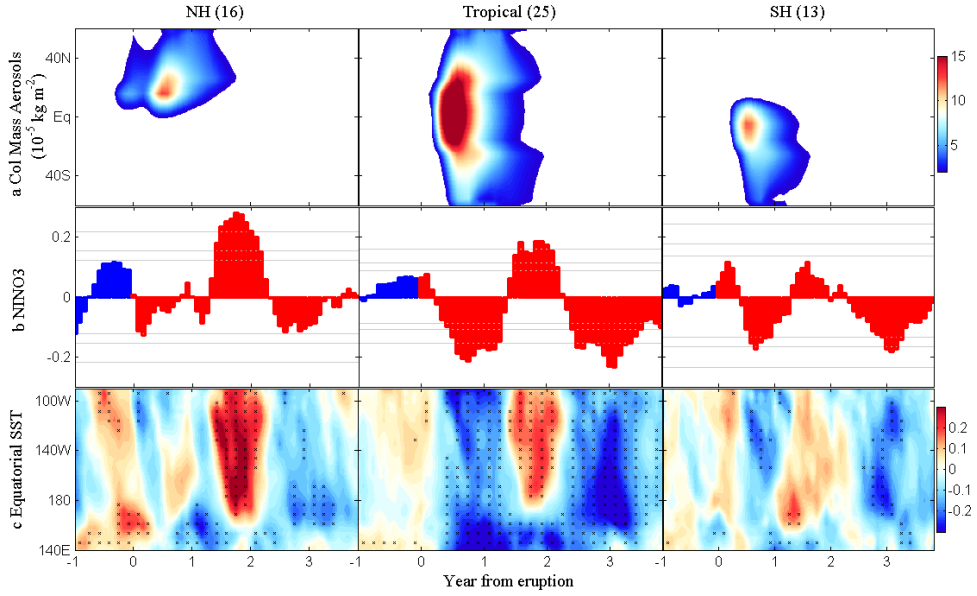

700

701 **Fig. 6** Model responses to different volcanic eruptions. Zonally-averaged aerosol
702 column density (**a**), normalized SEA results of NINO3 index (**b**), and equatorial (5^{o}S-
703 5^{o}N average) SST anomalies (**c**) are shown for 16 NH eruptions (left panels), 25 tropical
704 eruptions (middle panels), and 13 SH eruptions (right panels). Confidence limits (90%,
705 95%, 99%) are marked by horizontal lines for composite NINO3, and the equatorial
706 SST anomalies significant above the 95% confidence level are marked by stippling.
707 Blue and red bars mark the pre- and post-eruption years, respectively. "0" denotes the
708 year of each eruption, and "+1" indicates one year after the eruption.

709

710

711

712

713

714

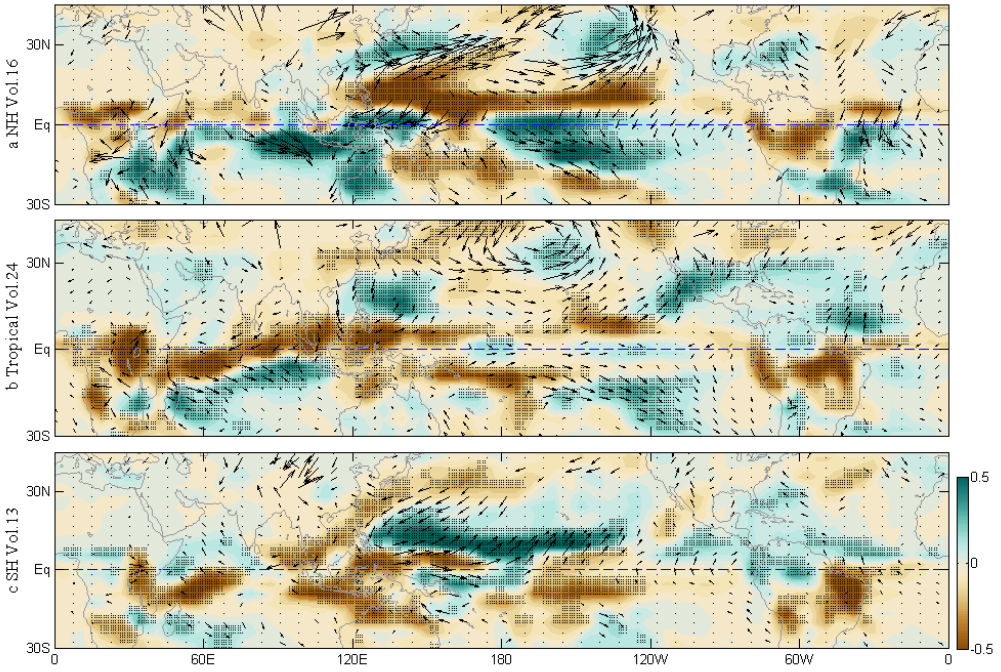

715

716 **Fig. 7** Spatial patterns of different volcano-forced modes. The normalized composite

717 precipitation (shading) and 850-hPa wind (vectors) anomalies are shown for the first

718 winter (December-February) after the NH (**a**), the tropical (**b**), and the SH (**c**) eruptions.

719 Stippling indicates the >95% confidence level based on the Monte Carlo resampling

720 (n=10,000). Only the wind anomalies above the 95% significance level are drawn.

721

722

723

724

725

726

727

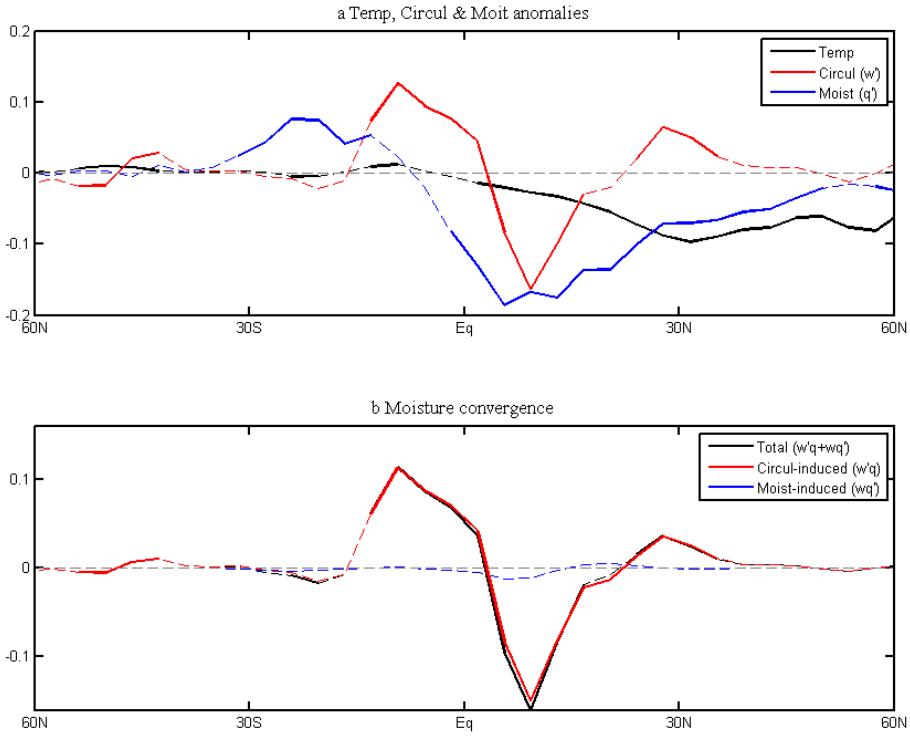

728

729 **Fig. 8** Meridional distributions of NH volcano-induced responses. The normalized
730 composite zonal-mean anomalies of (**a**) surface temperature (dark line), 500-hPa
731 vertical velocity (w', red line) and 850-hPa specific humidity (q', blue line), and (**b**)
732 total moisture convergence (w'q+wq', dark line), circulation change-induced moisture
733 convergence (w'q, red line), and moisture change-induced moisture convergence (wq',
734 blue line) are shown for the first winter (December-February) after the NH eruptions.
735 Prime denotes the anomaly, and anomalies above the 95% significance level are shown
736 by solid lines.

737

738

739

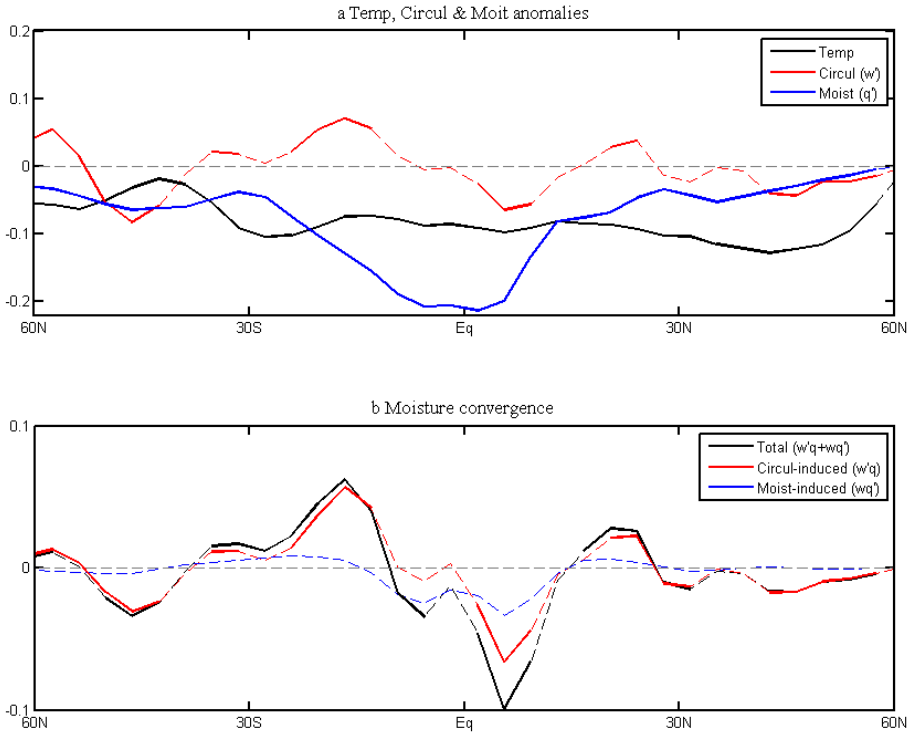

740

741 **Fig. 9** Same as Fig. 8, except for the tropical eruptions.

742

743

744

745

746

747

748

749

750

751

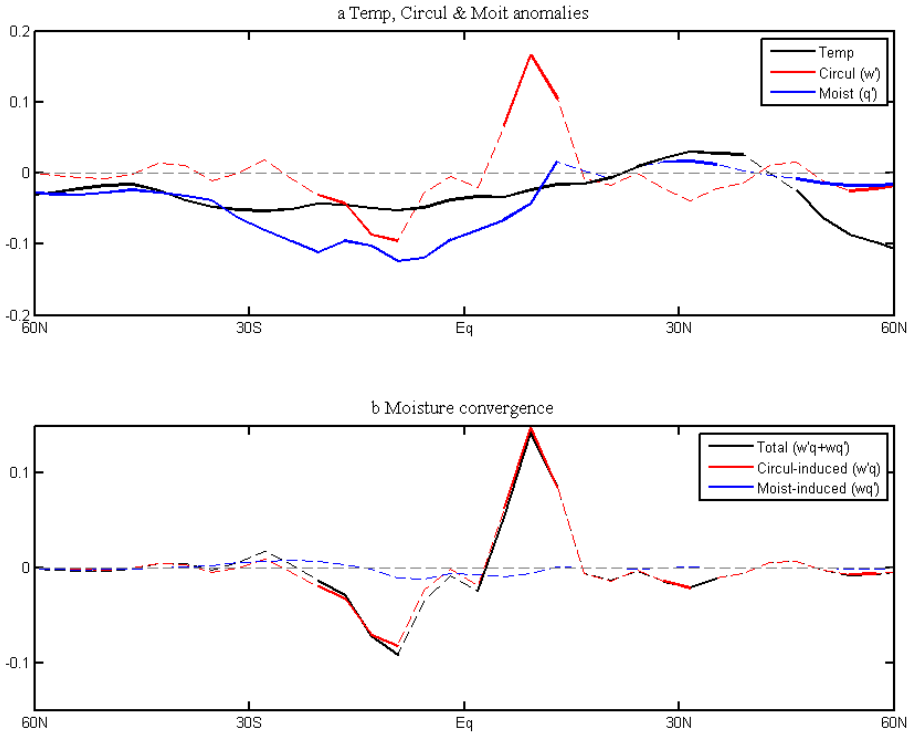

752

753 **Fig. 10** Same as Fig. 8, except for the SH eruptions.

754

755

756

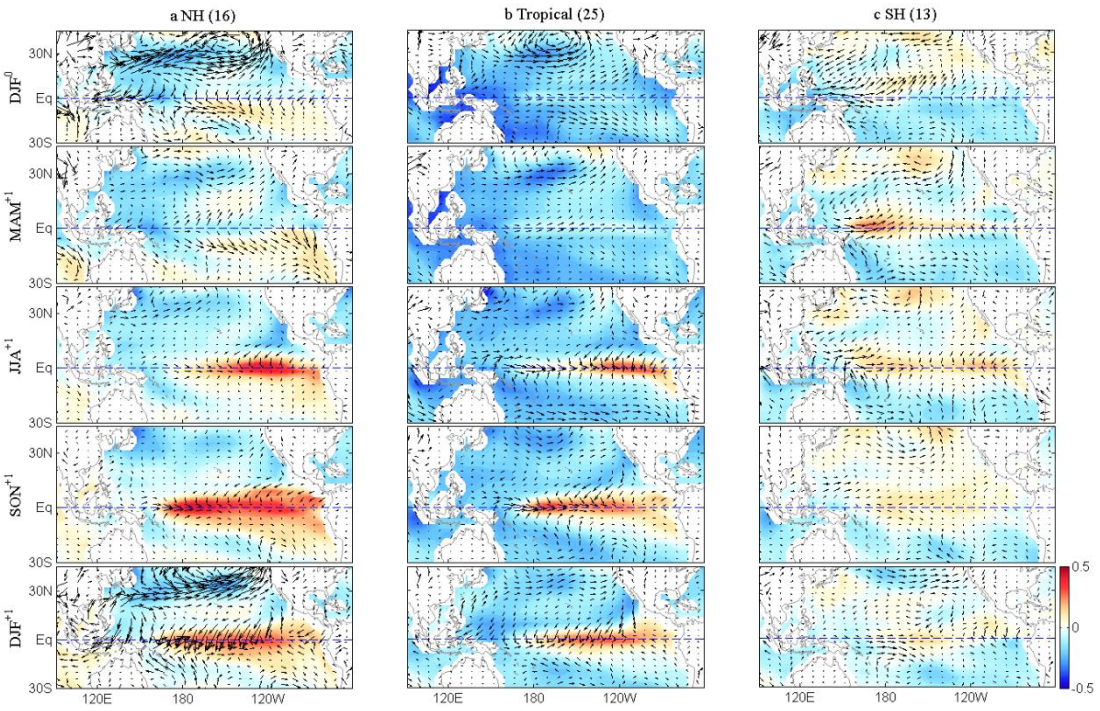

Fig. 11 SST anomaly evolutions after different eruptions. The composites of normalized three-month-mean SST anomalies (shading) and 850-hPa wind anomalies (vectors) since the first winter after the NH (**a**), the tropical (**b**), and the SH (**c**) eruptions. "0" denotes the year of each eruption, and "+1" indicates one year after the eruption.

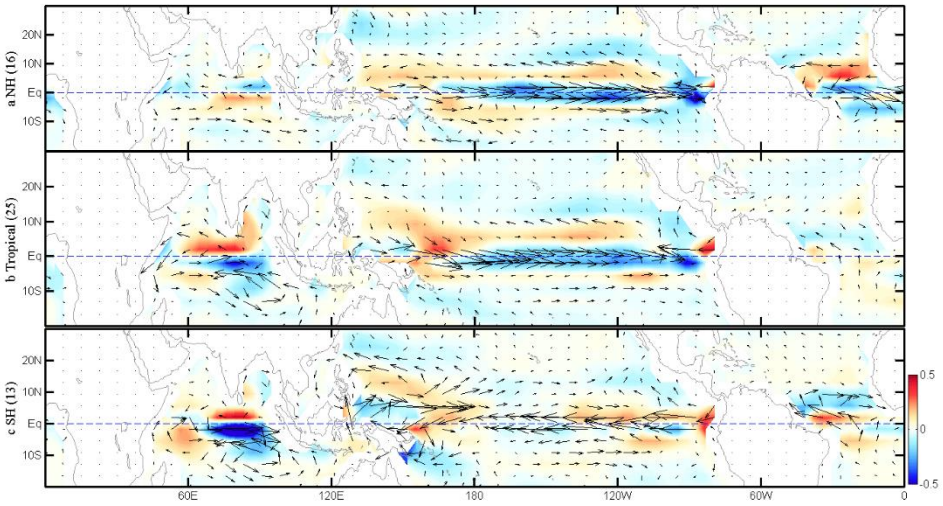

Fig. 12 Different oceanic responses to different eruptions. The normalized composite summer-mean (June-August) surface currents and surface (0-20 m) upwelling anomalies one year after the NH (**a**), the tropical (**b**), and the SH (**c**) eruptions.

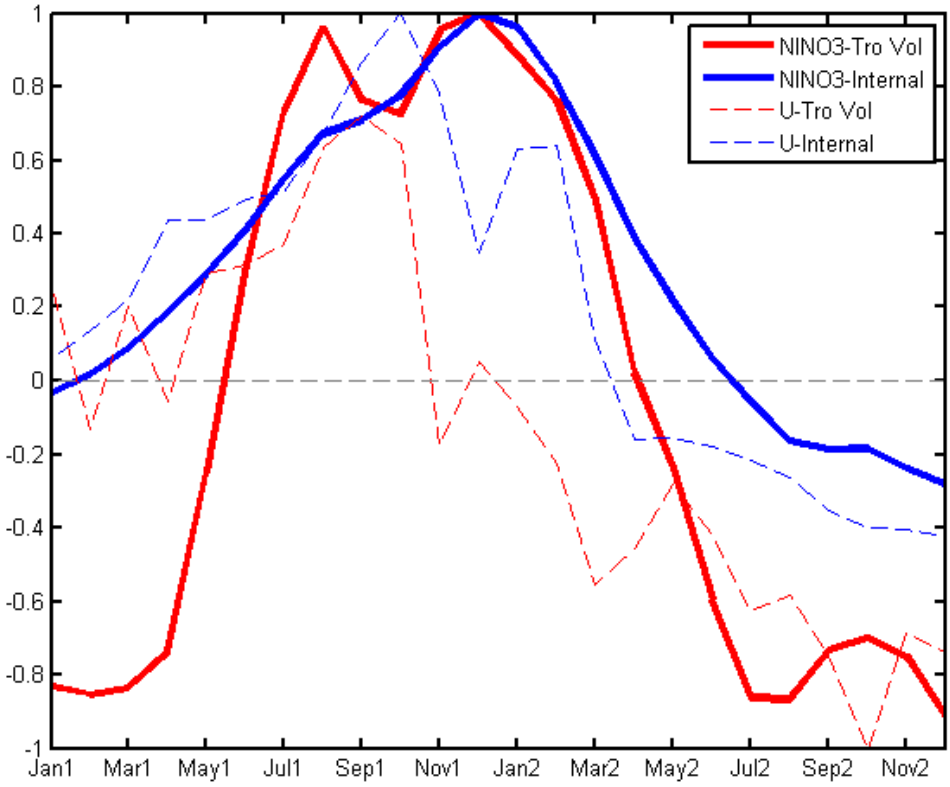

783

784 **Fig. 13** Transition to La Niña from tropical eruption-induced El Niño mode and internal
785 El Niño mode. Shown are the composite NINO3 index for 25 tropical eruptions (thick
786 red line) and for the El Niño in the control run (thick blue line), as well as the associated
787 zonal wind anomalies (dashed lines) averaged over the western Pacific (5^{o}S-5^{o}N,
788 120^{o}E-150^{o}E). "1" denotes one year after each eruption, and "2", two years. The El
789 Niño in the control run is defined when the boreal winter (December-February average)
790 NINO index is above one standard deviation. Each variable is normalized by its
791 maximum value in years "1" and "2".

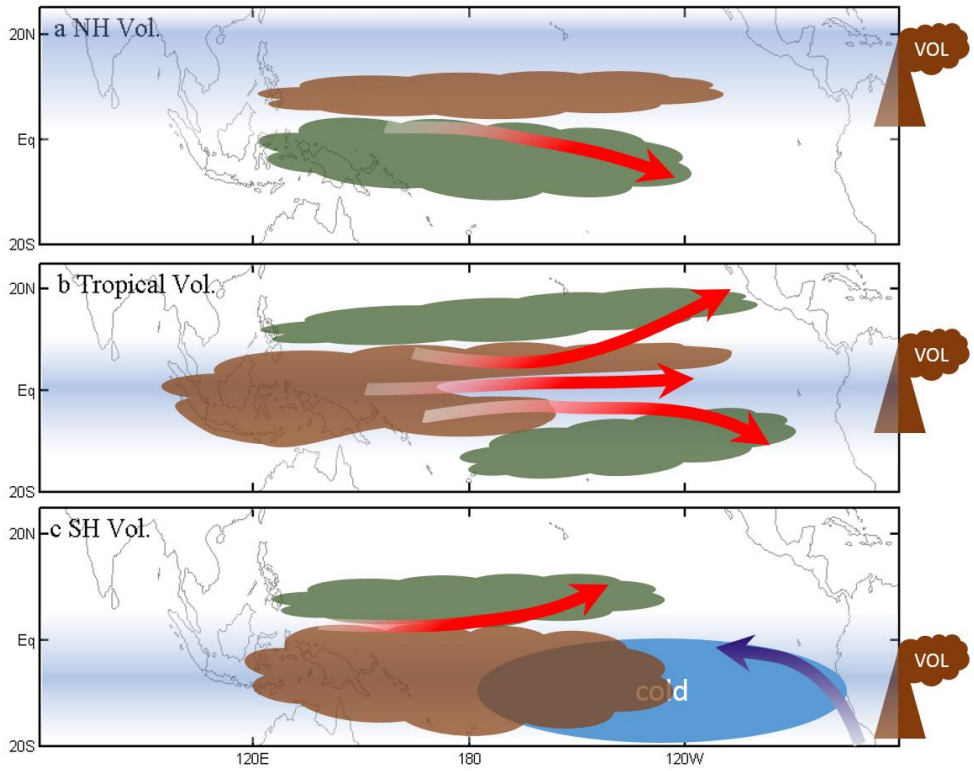

792

793 **Fig. 14** Schematic diagram showing different eruption-induced responses. Shown are
794 surface cooling (blue shading), precipitation anomaly (cloud), and surface wind
795 anomaly (vector) in the first boreal winter after the NH eruptions (**a**), the tropical
796 eruptions (**b**), and the SH eruptions (**c**). Positive/negative precipitation anomaly is
797 denoted by green/brown cloud. The blue ellipse denotes the southeast Pacific cooling.

798